Optical and photoluminescence performance of electrodeposited arsenic selenide thin film doped with erbium ion

Dr. Sudhir Kumar Mishra,

Principal,
S.S. College, Jehanabad,

Abstract*: The solid state performance of Erbium ion (Er^{3+}), a rare-earth ion, incorporated into the lattice of arsenic selenide (As_2Se_3) film is here presented. By varying the concentration of the dopant from 1 to 5% (wt.%), the films were deposited on a fluorine-doped SnO_2 glass via the electrodeposition method. The structural, optical and morphological characteristics of the samples were obtained using the XRD and Raman spectroscopy, UV-VIS-NIR and photoluminescence spectroscopy and scanning electron microscopy respectively. Polycrystalline films having monoclinic and cubic crystal structures for the undoped and doped samples respectively were observed from the XRD analysis. 34.5 nm and 44.2 nm were estimated for the mean grain size of the undoped and doped films respectively. The Raman spectra revealed the diffusion of the Erbium ion (Er^{3+}) into the As_2Se_3 lattice by Raman shift. The films revealed least absorbance and high transmittance up to 99% in the IR region with increasing doping. A high refractive index value of 2.66 was observed for all the films with a broadening towards the NIR region. The energy bandgap was estimated and lies in the range of 3.61–3.85 eV which slightly decreased with increasing doping concentration. The PL spectra showed intense excitonic (near-edge) emission bands at 348 nm with increasing doping. SEM micrographs revealed fairly homogeneous nano-ball morphology at lower doping concentration and nanoclusters at higher doping concentration. Annealing of the films above the glass-transition temperature (*Tg*) allowed the transition of the film to the crystalline phase which is an interesting feature in binary chalcogenide-based phase change memory (PCM) photonics devices.

Introduction

Global attention has recently been drawn to research in the domains of solid state integrated optics with integrated photonics (IPs) – a close analogy to integrated electronics, being a key area of interest [1]. Integrated electronic circuits are known for limitations such as high power consumption due to energy loss of the electrons during energy transfer mechanisms, thereby releasing virtually all the energy they possess. On the contrary, photons which are the key players in integrated photonics are known to travel with the speed of light with minimal loss of energy during energy transfer mechanisms hence are able to transmit large amounts of information at much higher speeds[2]. A major target in photonics is to integrate several opto-electronic components onto the computer chip with a summed-up advantage of higher transmission speed, lower consumption of power and also compatibility with the Complementary Metal-oxide Semiconductor (CMOS) technology [3].

Phase-change memory (PCM) device synthesized from chalcogenide materials, as a class of photonic devices, has attracted research interest recently in non-volatile memory (NVM) photonic applications [4–6]. PCM device possesses interesting qualities for use in NVM data storage and information dissemination by promptly inter-switching its amorphous and crystalline phases [7]. Chalcogenide compounds which elements of groups IV and V like Germanium (Ge) and Arsenic (As) respectively, have shown promising features for use as optical materials in integrated photonics more especially in PCM applications [6,8]. But it's not limited to just PCM, it can be used also in others applications such as high-quantum output luminophores [9,10], optical filters [11], optical waveguide [12], active media in Laser technology [13], etc. this is due to the visible emission observed through the photoluminescence spectra. In technical terms, Fischer in his work, has referred to these elements as Chalcogens in the case where the adjacent elements nor their compounds are absent [14].

Chalcogenide-based PCM (cb-PCM) films such as arsenic selenide (As_2Se_3) – our material of interest – appear in two phases: amorphous and crystalline phase which depends on the propaedeutic conditions like glass-transition temperature (T_g), composition of reacting specie, deposition technique, etc. The amorphous form has attracted significant attention over time as potential source materials for IPs such as optical waveguides, Infrared lasers, phase-change memory (PCM) device among others. This is due to their high refractive index, high non-linearity indices, NIR transparency, structural stability over time [15]. Furthermore, in recent times, metal chalcogenide materials with wide band gap energies such as As_2Se_3 have shown promising features for applications in non-linear optical devices operating in the infrared window of the electromagnetic spectrum [16]. Researchers have vividly noted how the solid state properties of these chalcogenide materials are noticeably influenced by incorporation of dopants into the lattice network of the host material [17]. In addition, their low-phonon energies coupled with high refractive index marks them out as viable host for rare-earth (RE) doping [18].

Conventional techniques have been adopted to synthesize cb-PCM films which include atomic layer deposition [19], thermal evaporation [20], pulsed layer deposition [21], spin-coating [22],and RFsputtering [23], which are all vacuum based techniques and expensive to handle. Hence, the alternative simple electrodeposition technique was adopted for this work due to its relative ease of use with less complexity, cost-effectiveness [24], less deposition time, film thickness and size control and ability to reproduce films. In addition, electrodeposition from aqueous or non-aqueous solutions has been used to deposit crystalline chalcogenide films mainly for phase-change memory (PCM) and solar-cell applications[25].

In this work, we embarked on growing the crystalline phase of the cb- PCM film doping with Erbium ion via the electrodeposition method while annealing a little above the T_g of As_2Se_3 with a reported value of 170° C [26]. However, rarity of detailed literary documentation of the crystalline phase cb-PCM doped with Erbium ion synthesized by electrodeposition technique and their possible application in integrated photonics greatly drives this research work.

Experimental procedure

Chemicals of analytical grade requiring no further purification for their usage were utilized in this work. These include Arsenic trioxide (As_2O_3, 99.98%), Selenium (Se, 99.98%) metal, Erbium trioxide (Er_2O_3, 99.8% [procured from Sigma-Aldrich]), distilled water, ethanol, acetone and hydrochloric acid. Commercially procured Fluorine-doped SnO_2 (FTO) glass slides served as the working electrode (substrate) connected to a dc voltage potentiostat in a 3-electrode cell system for film deposition. The substrates were pre-cleaned in an ultrasonicator at an operating temperature of 37° C using distilled water in the first cleaning step. Ethanol and acetone were afterwards used to degrease the surface from contaminants while finally rinsing in distilled water before use for deposition. Each treatment step was performed respectively for 15 min.

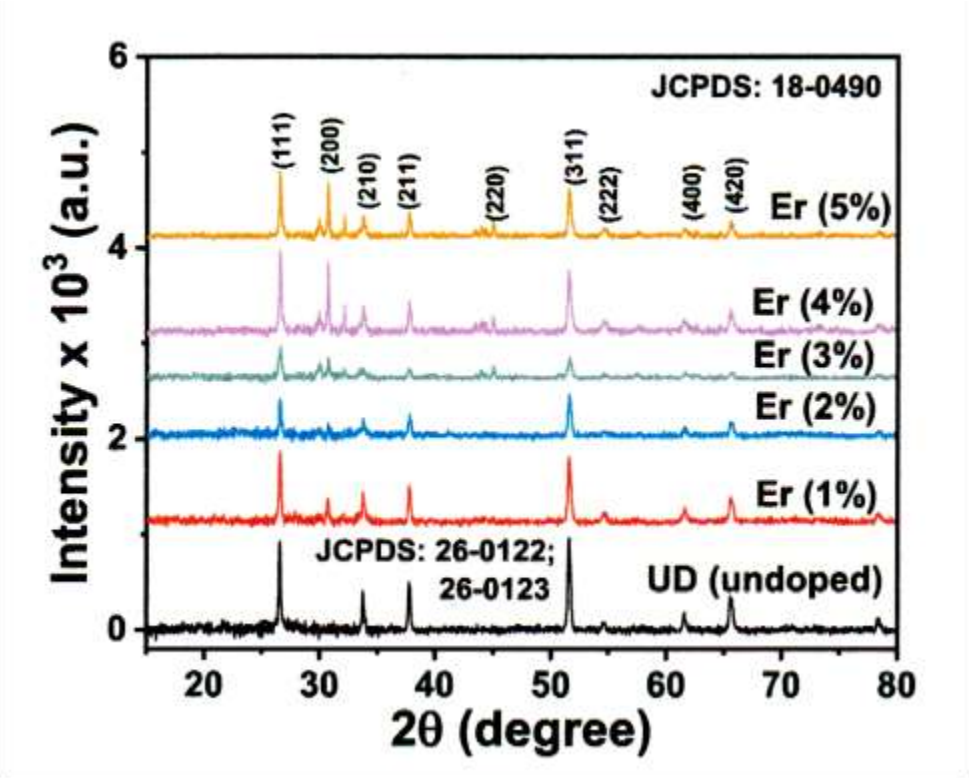

Fig. 1 Stacked XRD plot of films at varying doping concentration.

The precursor solution was prepared by using 2.5 ml of 0.3 M HCl to dissolve 0.1 M As_2O_3 and 0.1 M Se in separate containers while using distilled water to make up to 100 ml of solution. Continuous stirring for 10 min was done to enhance dissolution and uniform distribution of the reactants. The solutions were mixed in the volume ratio of 1:1 in a 50 ml beaker and deposited on the pre-cleaned glass of sheet resistance, 23 Ω/sq. Dissolving the dopant, Er_2O_3 in 100 ml of distilled water and varying its concentration from 1 to 5% (wt.%), the films were respectively deposited at room temperature in the ratio of 2:2:1 with a dc voltage supply of 10 V for 5 s.

The as-grown films were annealed for 1 h at a temperature of 200° C in a resettable blast oven in order to improve the film quality and crystallinity of the films. This heat treatment performed to remove the absorbing oxides and to achieve films of high purity have earlier been accounted by Ref. [27]. The samples were afterwards studied for structural, optical and morphological properties using the X-ray diffractometer (XRD) and Raman spectroscopy, UV-VIS-NIR and photoluminescence spectroscopy and scanning electron microscopy (SEM). The XRD patterns were recorded using a Bruker D2 phaser table-top model diffractometer in the 2θ scanning range of 15–80° while the Raman spectra was collected using LabSpec6 (Horiba Scientific) Raman microscope in the backscattering geometry with a spectral resolution of 0.3 cm^{-1} at ambient temperature. A He–Ne laser of λ = 633 nm and a power level of 2 mW was employed. The lower power have been chosen in order to prevent any photo-induced effect [28]. The same microscope was used to obtain the PL data at an excitation wavelength of 325 nm. The UV-1800series Shimadzu spectrophotometer in the wavelength interval of 200–1100 nm was used to obtain the optical data. The Jeol, JSM 7000 series Scanning electron microscope was used to obtain the morphological micrographs of films at 15.0 kV scan voltage.

3. Results and discussions

3.1. XRD studies

The diffraction patterns in Fig. 1 revealed films of polycrystalline nature. Predominant peaks at crystal orientation of (110), (015), ($\bar{2}$ 25) and ($\bar{1}$ 62) were observed for the undoped film which corresponds to 26.52°, 37.77 °, 51.58 ° and 61.52 ° 2theta values respectively. Re-orientation of crystal planes was observed with incorporation of Erbium doping with prominent peaks (111), (200), (211), (311) and (420) at exactly 2theta values of 26.56 °, 30.63 °, 37.80 °, 51.52 ° and 65.46 °. However, with increasing molar concentration of dopant, other minor peaks were found to be present. We hereby presume that this could have resulted from background signals detected from the substrate material. Also worthy of note is that at Er (3%), critical peak reduction was observed which indicates that the films could probably attain an amorphous form at this concentration.

Table 1

Summarized lattice parameters for films.

Sample	2Theta (2θ°)	Lattice spacing, d (Å)	FWHM (β rad)	Crystallite Size, D (nm)	Dislocation density (δ) (lines/m2) x 10^{15}	Lattice Strain, (ε) x 10^{-3}
UD	26.52	3.3583	0.0041	34.5	0.84	4.38
Er1	26.56	3.3533	0.0037	38.1	0.68	3.96
Er2	26.56	3.3533	0.0037	38.1	0.68	3.96
Er3	26.56	3.3533	0.0037	38.1	0.68	3.96
Er4	26.55	3.3545	0.0037	38.0	0.69	3.97
Er5	26.54	3.3558	0.0038	37.8	0.69	3.99

The undoped films exhibited monoclinic crystal structure (JCPDS card nos.: 26–0123 and 26–0122 [29]) while cubic structure (JCPDS card no.: 18–0490) for the doped samples. The observed cubic structure transformation at elevated temperatures have been reported by Ref. [30] while also noting that at room temperature the dopant possesses the α-phase hexagonal closed packing (hcp) structure.

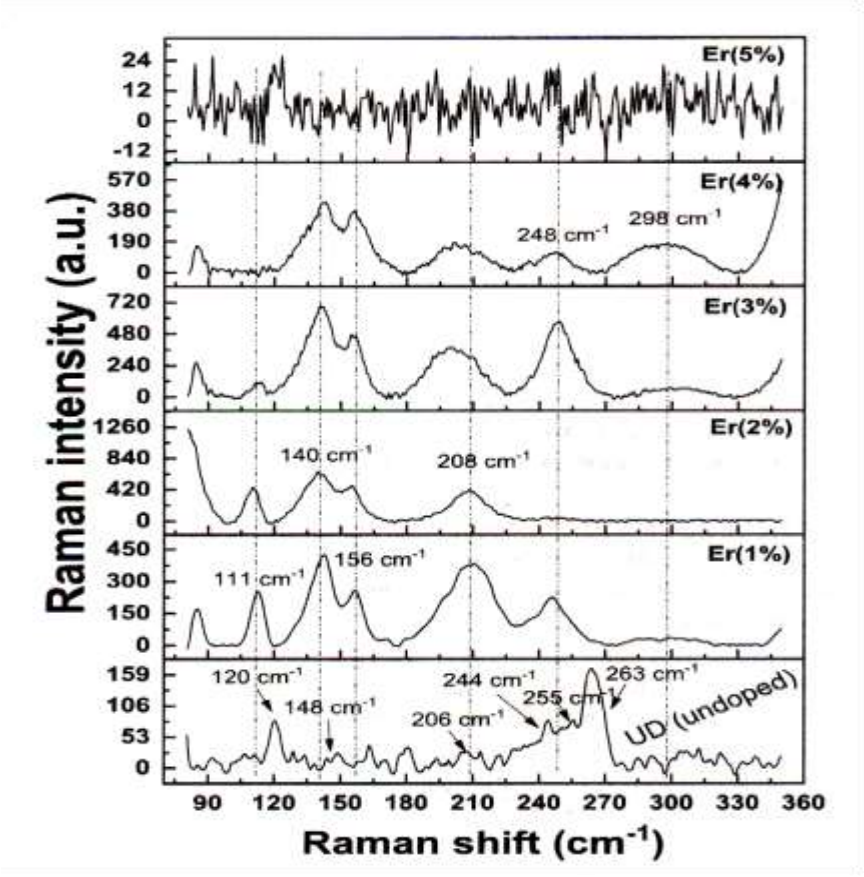

Fig. 2 Raman Shift of films at varying concentrations.

The crystallite size ($D = \frac{K\lambda}{\beta Cos\theta}$ = [31]), inter-planar spacing (d = $\frac{\lambda}{2sin\theta}$), dislocation density $\left(\delta = {}^{1}/_{D^2}\right)$ and lattice strain $\left(\varepsilon = {}^{\beta}/_{4\tan\theta}\right)$ [32] were estimated at the prominent 2theta value and reported in Table 1. The slight increase in the average size of crystallites indicates the presence of lattice strain, however infinitesimal the value, in the host material's lattice structure. This is in accordance with the report of researchers that the non-uniformly distributed inter-planar spacing and interstitial impurities in the sample contributes somewhat to the micro strain [33] alongside temperature term, faulting and cracks.

3.2. Raman studies

The modes of vibration at various frequencies (wavenumbers) of unique molecular groups of the undoped and Erbium-doped samples are presented in the Raman shift spectra in Fig. 2.

The peaks of 148 cm $^{-1}$ and 255 $^{-1}$ cm are attributed to the vibration of covalent bonds in Se_8 rings and to the bending modes in Se units [34, 35], the peak of 208 cm $^{-1}$ is attributed to As_4Se_4 cages [36] and the peaks of 244 cm $^{-1}$ and 263 cm^{-1} are attributed to As–Se–Se–As dimers [37]. However, the peak located at 120 cm^{-1} in UD is not identified which is probably attributed to structural units containing As–As bonds [36] and whose shift to 140 cm^{-1} for the doped samples indicates diffusion into As_2Se_3 lattice network except at Er (5%) where it disappeared [38].

After introducing of small amounts of Erbium ions, the most of the peaks observed in UD disappear and new phonon modes attributed to new structures appear. This substantial change in Raman spectra confirms the formation of new structural units consisting of both As and Se atoms [36]. The three peaks of 244 cm^{-1}, 255 cm^{-1} and 263 cm^{-1} disappear, however, a new high peak is observed at 208 cm^{-1}, this peak is related to the molecules of As_4Se_4 cages, observed at 206 cm^{-1} in UD; the shift is expected when the composition is highly altered. This can be explained by the breaking of Se bonds in the Se_8 rings and As–Se–Se–As dimers and in turn, the formation of more As-rich network with the formation of monomeric As_4Se_4 cages based on realgar –type structure [6]. But, this peak decreases and becomes broader, after introducing 2% of Erbium, even, it splits to three broad bands located at 200 cm^{-1}, 248 cm^{-1}, 298 cm^{-1} after introducing 3% and more of Erbium into the matrix; this change explains the disorder of Se–Se chains and consequently the presence of an amorphous phase in the matrix. This is also explained in the XRD result for the Erbium doping at 3% concentration which nearly attains its amorphous form at this concentration.

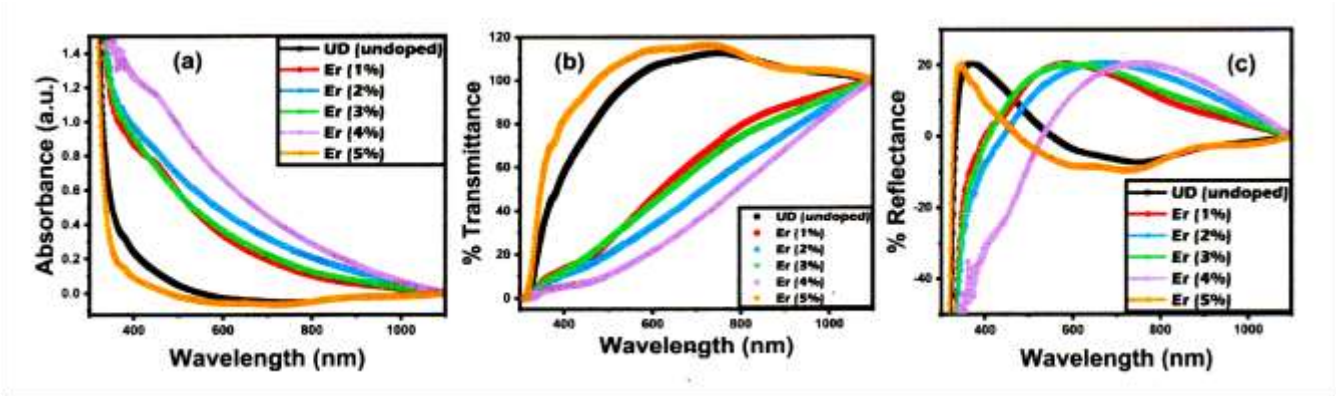

Fig. 3. (a) Absorbance (b) and (c) Reflectance plots of Er-doped As_2Se_3

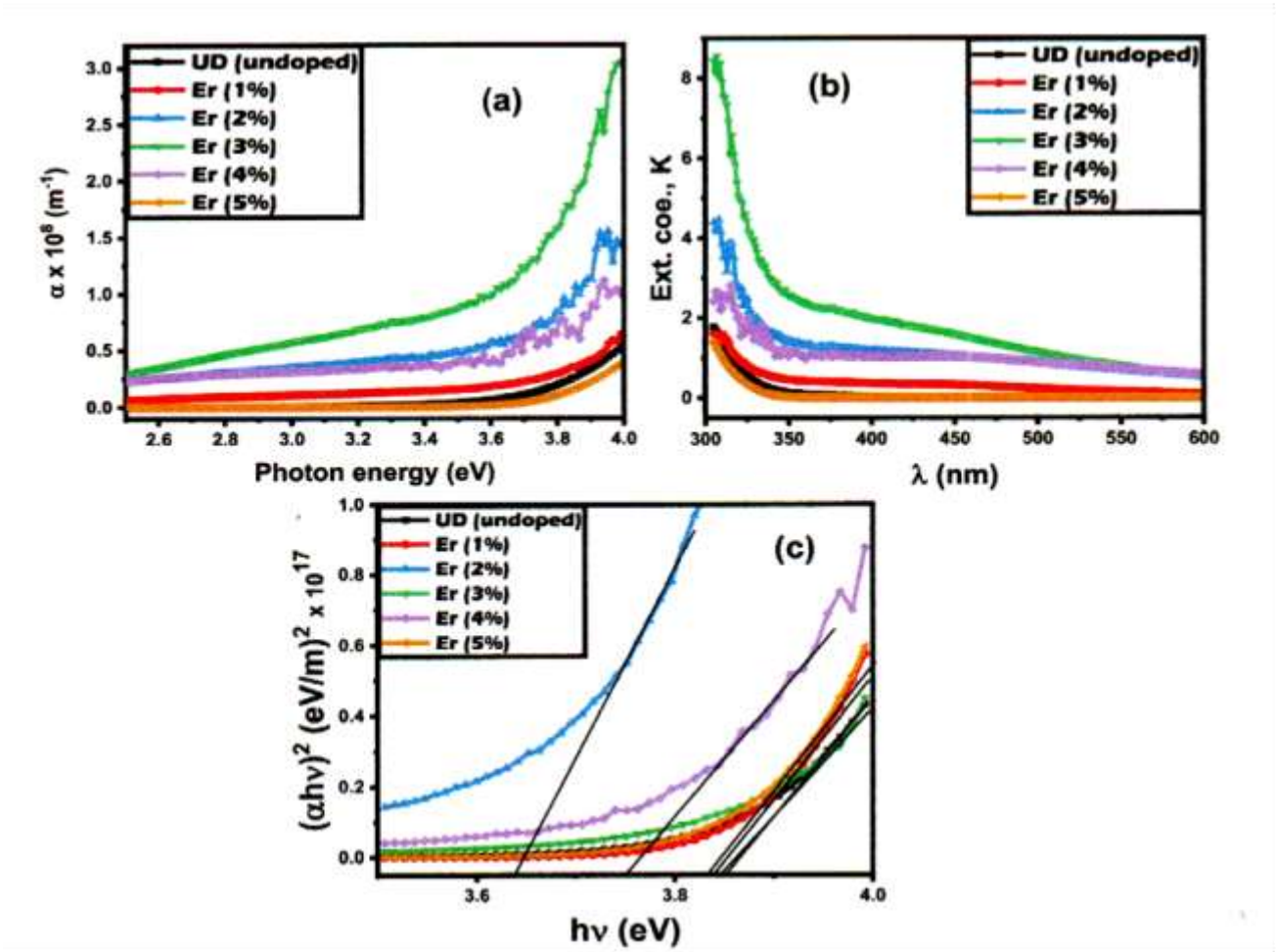

Fig. 4 (a) Absorption coefficient (b) Extinction coefficient (c0 Energy band gap plots of films

Another three peaks appear when we introduce 1% Erbium; the first two peaks are located at 140 cm^{-1} and 156 cm^{-1}, and these are close to the peak located at 148 cm^{-1} of Se_8 ring, the two peaks could be attributed to $AsSe_3$ pyramidal units. $AsSe_3$ is formed after the breaking of As–As or Se–Se bonds in As and Se rich units. We can observe a shift of the peak at 156 cm^{-1} toward lower energies for the Erbium concentration of 1%–4% with total disappearance of peaks at 5%. A similar trend of peak disappearance with increasing thickness due to doping was observed for $Si_{0.5}Ge_{0.5}$ on a GaAs surface [39]. In their quantitative study of the composition dependence of the peak position of $AsSe_3$, Yang et al. showed that the peak of $AsSe_3$ modes shifts toward lower energy when As content increase from 0 till 0.4 and it shifts toward higher energies when As content increase from 0.4 to 0.6 [40]. This shift evolution is consistent with what we observed in XRD, see Fig. 1, where the 3% presents a very low crystallinity. The third peak is located at 111 cm^{-1}, which could be attributed to the As_4Se_4 or As_4Se_3 cages, because it presents the same behaviour of the peaks located at 208 cm^{-1}.

3.3. Optical studies

3.3.1. Absorbance, transmittance and reflectance plots

The absorbance, transmittance and reflectance spectra of the film in the wavelength range of 300–1100 nm obtained at room temperature is presented in Fig. 3 (a - c) respectively.

The absorbance plots in Fig. 3a revealed highest absorption of all the samples in the UV region, lower absorption in the visible region and least absorption in the infrared region. It was also observed that the absorption edge red-shifted slightly towards the longer wavelength region (lower energy) from 322 nm to about 350 nm with increase in the doping concentration.

The transmittance values were calculated from the absorbance (A) values using the optical relation between transmittance (T) and absorbance (A): $T = 10^{-A}$*:* The samples showed significant rise in transmittance with increasing doping concentration and wavelength. Generally, there was a pronounced increase in the transmittance up to 99% in the NIR region (770–1100 nm). This is an interesting property for devices with applications in the IR region such as the IR lasers, optical waveguides and bio-imaging devices. The reflectance (R) values were estimated from the optical parameter relation: $A + T + R = 1$ [41]. The doped films in the range of 1 – 4 wt%Er showed a maximum value of 20% reflectance. However, at higher concentration of 5 wt%Er, material presents

a very low reflectance, making it a suitable optical material for anti-reflective coating applications in the visible region (450–700 nm).

3.3.2. Absorption coefficient (α), extinction coefficient (K) and energy band gap (Eg) plots

Fig. 4 (a – c) shows the absorption coefficient, extinction coefficient and energy band gap, E_g of the films. The absorption coefficient was plotted against the photon energy and shows an increase with photon energy. The absorption coefficient was estimated from the reflectance (R) and transmittance (T) values given by equation: $\alpha = \frac{1}{d} ln\left(\frac{(1-R)^2}{T}\right)$ [42]

Also of note is the high dependence of the absorption coefficient on the dopant concentration. The undoped film showed an α-value of 0.74 x 108 m^{-1} while the film composed of 3% molar concentration showed a peak absorption coefficient value of 3.06 x 108 m^{-1} while 5% approached the same value of the undoped film at 0.52 x 108 m^{-1}. The extinction coefficient of the film was calculated using the equation: $K = \frac{\alpha\lambda}{4\pi}$ [43]. The plot of extinction coefficient against wavelength for the Erbium doped film at various percentage molar concentration is shown in Fig. 3b. It is seen that the extinction coefficient decreases with increasing wavelength for all the samples. This shows that the samples have high extinction coefficient in the UV region and low values in the IR region. This is attributed to the high absorption of the films in the UV region. However, film at 3% was observed to have the highest *K* value which also is in consonance with the XRD result with a consequent reduction in crystallinity of the film at this concentration.

Table 2 Summary of energy band gap (*Eg*) of films.

Sample label	Band gap, *Eg* (eV)
UD	3.85
Er1	3.83
Er2	3.61
Er3	3.73
Er4	3.77
Er5	3.83

The optical energy band gap, E_g was calculated using the Tauc equation: $(\alpha h\upsilon)^{1/n} = \beta(h\upsilon - h_\upsilon)$ [44], where $h\upsilon$ = photon energy, β = band tailing parameter, E_g = energy band gap, n = transition mode power factor, where n = ½ is for allowed direct transition. The plot of $(\alpha h\upsilon)^2$ against hυ produces a straight line in a particular region whose extrapolation along the $h\upsilon$ -axis intercepts where α = 0, gives the value of the optical energy band gap. It is evident from the band gap values in Table 2 that the Er doping induced the band gap narrowing. This is due to the many-body interaction effect between the free charge carriers and the ionized impurities (dopants). Conduction band tail has also been noted to contribute to band gap narrowing [45].

3.3.3. Refractive index (n) and optical conductivity (σ_{opt}) studies

The non-linear refractive index, n and optical conductivity, σ_{opt} plots of the films are presented in Fig. 5 (a & b) respectively. The refractive index was estimated from the reflectance (R) and the extinction coefficient (K) values using equation: $n = \frac{1+R}{1-R} + \sqrt{\frac{4R}{(1-R)^2} - K^2}$ [32]. A peak value of 2.66 was recorded for the refractive index of all the films. However, higher doping concentration led to the broadening of the spectra from the visible to infrared region where it terminates at a value of 0.98. This is fairly close to the refractive index value of 2.83 obtained by Ref. [8] for the undoped As_2Se_3 sample which increased to 2.93 after exposure to light. A closely similar result of 2.7 for the refractive index of solution-phase deposited As_2Se_3 which reached a saturation point after annealing at 150 °C was obtained by Ref. [46]. The non-linear nature of the refractive index indicates a shift from normal dispersion behaviour of the material. This indicates that the refractive index of the material does not depend on the wavelength on a linear scale.

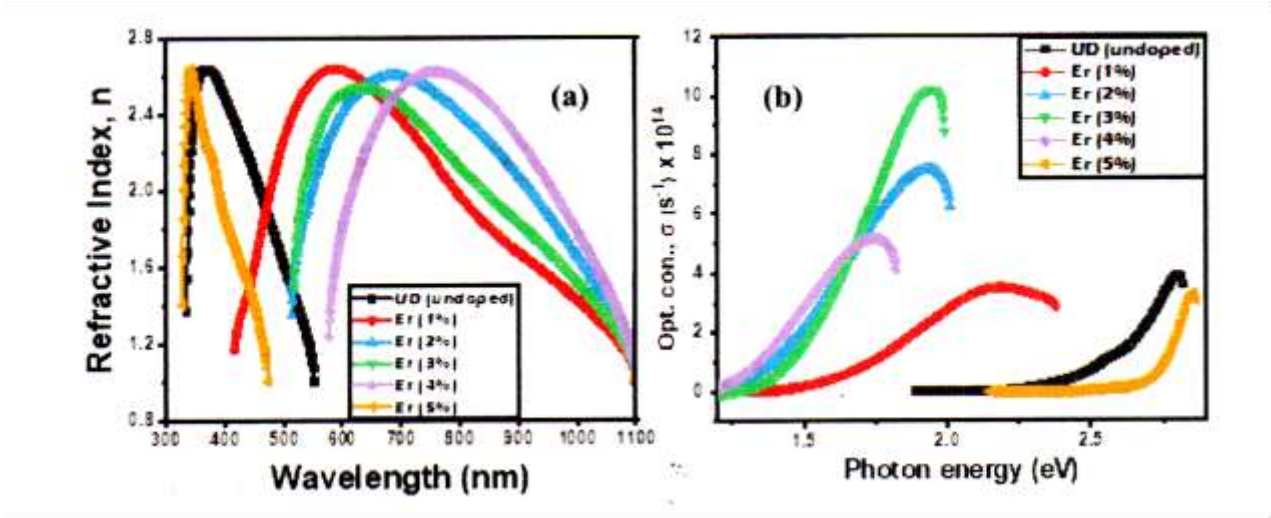

Fig. 5 (a) Refractive index (b) Optical conductivity plots of films.

It is most convenient to express the optical response of a given material in terms of its optical conductivity (σ_{opt}). The optical conductivity was estimated from the relation: $\sigma_{opt} = \frac{\alpha nc}{4\pi}$ [47] and plotted against the photon energy of the films as shown in Fig. 5 (b) and shows that the optical conductivity (σ_{opt}) values of the undoped films rose from zero level to a peak value of 3.94 x 10^{14} s^{-1} at 2.8 eV with increasing photon energy. On introduction of Er dopant into the matrix of the undoped film, we observed a significant increase in the optical conductivity of the films. Er (3%) showed the highest σ_{opt} value of 10.36 x 10^{14} s^{-1} at 1.94 eV which is more than twice the value of the undoped film while Er (5%) showed a σ_{opt} value of 3.42 x 10^{14} s^{-1} close to the value of the undoped film at roughly the same energy point. The high σ_{opt} value of Er (3%) is attributed to its high absorption value as earlier reported in this work which consequently leads to self-quenching (photo-quenching). This is correlated with the reduction in intensity as shown in the XRD patterns in Fig. 1. This photo-quenching is attributed to the electric dipole-quadrupole interaction [48].

In addition, a critical investigation was made at photon energy value which lie at the mid-way (1.90 eV) of the mean energy band gap (E_g = 3.80 eV) value of the undoped and doped films. We observed that the undoped film returns negative σ-values at this energy point. Consequently, the absorption coefficient (α) returns a negative value. This is perhaps interpreted to mean that the films at this energy point do not possess quite enough capacity to allow the passage of photons through the material. On the other hand, the Er-doped films at this energy point returns high and positive σ-values for low doping concentrations and zero σ-values for concentrations greater than 3%.

3.3.4. Photoluminescence (PL) studies

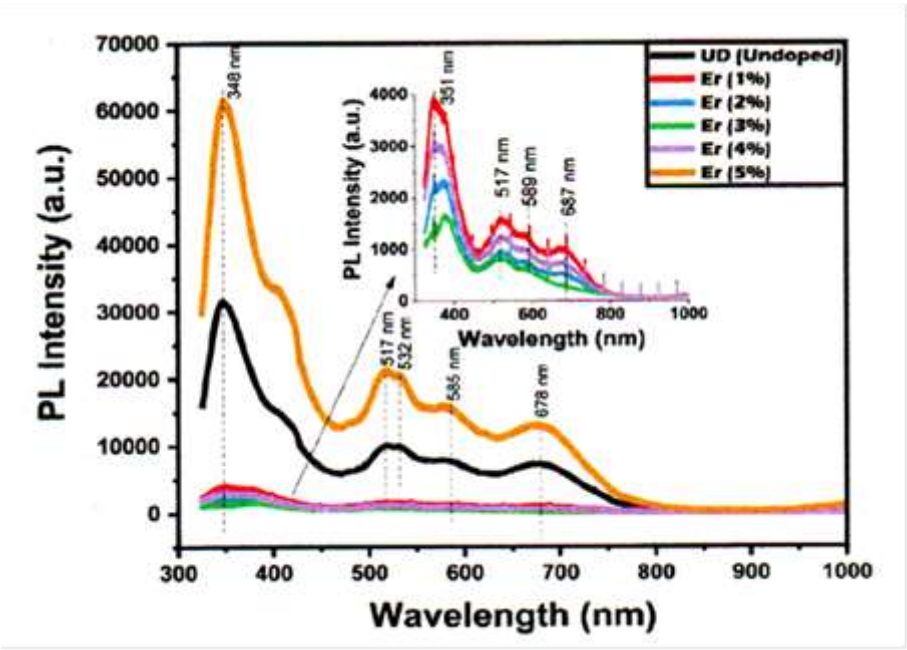

Fig. 6. PL spectra of films [inset: scaled view of Er (1%), Er (2%), Er (3%) and Er (4%)].

The photoluminescence (PL) spectra of the undoped and doped films are presented in Fig. 6. The excitation wavelength of the light source was set at 325 nm which has been intuitively chosen from the absorption edge of the UV-VIS absorption spectra earlier reported in this work. It is observed from Fig. 6 that Er (5%) showed the strongest PL emission peaks at 348 nm, 585 nm, 589 nm, 678 nm and 687 nm corresponding to $^4F_{3/2} \rightarrow {}^4I_{15/2}$, $^4G_{9/2} \rightarrow {}_4I_{15/2}$, $^2H_{11/2} \rightarrow {}^4I_{15/2}$, $^4S_{3/2} \rightarrow {}^4I_{15/2}$, $^4F_{9/2} \rightarrow {}^4I_{15/2}$ transitions in the *4f orbital* of the Er^{3+} ion. The highest luminescence observed in Er (5%) agrees well with the reports of [48,49] and finds interesting application in thermoluminescence dosimetry (TLD) and optical thermometry

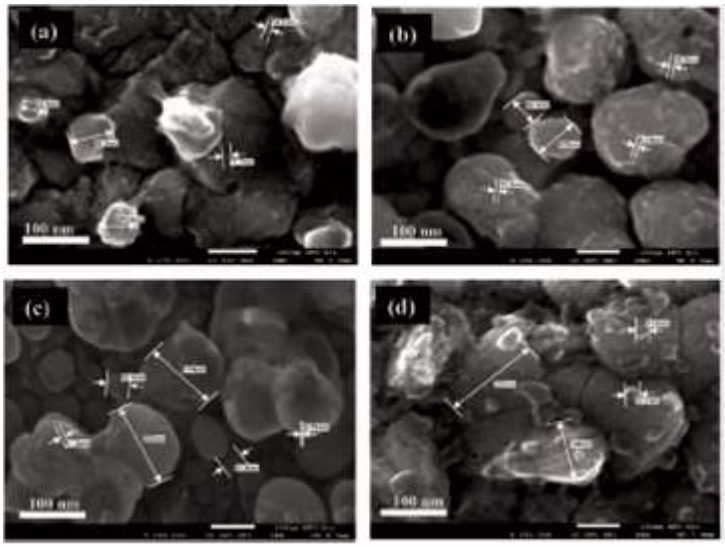

Fig. 7 SEMmicrograph of (a) undoped film (b) Er (1%) (c) Er (2%) (d) Er (5%)

The PL spectra in Fig. 6 is typical of a multimode transition spanning the UV and VIS regions of the electromagnetic spectrum. The emission bands at 348 and 351 nm depict near-edge (excitonic) emission while the other emission bands show the trapped emission type with low intensities. This is attributed to the fact that excitonic emission is usually sharp and located near absorption edge of the material, while the trapped emission is broad and Stokes-shifted (low-energy shift or down-conversion process) as noted by Ref.[50]. Two kinds of emission peaks are characteristic of nanocrystals: excitonic and trapped (delayed) emissions depending if the emission occurred at or near the band edge or otherwise respectively [51].

3.4. Morphological studies

The surface morphologies of the undoped and doped films are presented in Fig. 7(a–d). The SEM micrographs show fairly dispersed nano-ball structures. Film at Er (1%) showed fairly uniform, spherical and homogeneously dispersed nano-balls while film at 5% showed nano-clusters. The undoped film (UD) showed an average particle size of 50.02 nm, Er (1%): 40.40 nm, Er (2%): 82.60 nm & Er (5%): 109.00 nm. The spherical nature of the particles allows for better light trapping.

4. Conclusion

In this work, As_2Se_3 thin film was successfully deposited on an FTO glass substrate via solution phase electrodeposition technique. The rare earth ions were also successfully incorporated into the lattice of the host chalcogenide material. This is apparent from the presence of microstrain along the lattice and the reduction of peak intensities in the diffractograms. The presence of peaks indicates crystallinity of the films. The phase change to crystalline form was observed to be due to annealing above the glass transition temperature and the composition of reacting species. This transformation depicts suitability of this material for use as a source material for phase-change memory (PCM) device – a passive optical device, for data storage in photonic integrated circuits (PICs). The suitability of the films for PCM application is due to the observed high refractive index (2.66) at 780 nm and high transparency (>90%) of the films in the IR region (770–1100 nm). However, this property belongs to the doped samples in the range of 1 – 4 wt%Er while the film at 5 wt%Er presents attributes for anti-reflective coating applications – another passive optical material which is due to their low reflectance in the visible region (450–700 nm).

In addition, the SEM micrographs revealed nano-balls and nano-clusters with fairly homogeneous distribution while the Raman spectra revealed the Raman shift due to incorporation of Erbium ions into the As_2Se_3 network. The PL spectra revealed intense excitonic (near-edge) emission at 348 nm. Summarily, the synthesis technique adopted in this work, annealing temperature and doping with rare-earth ions in addition with, especially the optical results, reveal suitability of our material as a passive optical material for PCM and anti-reflection coating applications.

Acknowledgments

The author would greatly like to thanks to Prof. R.P.S. Chauhan, Rtd. HOD, Deptt. Of Chemistry, M.U., Bodh Gaya, Prof. Sanjay Kr. Asso. Prof., Deptt. Of Chemistry, Jagdam College, Chapra, Prof. Rabindra Singh, HOD, Deptt. Of Chemistry, J.P.U., Chapra for their generous support and Technical helps accordingly.

References

1. L. Thylien, L. Wosinski, Integrated photonics in the 21st century, Photonics Res. 2 (2) (2014) 75.
2. D.J. Milliron, S. Raoux, R.M. Shelby, J. Jordan-Sweet, Solution-phase deposition and nanopatterning of GeSbSe phase-change materials, Nat. Mater. 6 (5) (May 2007) 352–356.
3. S. Raoux, W. Wełnic, D. Lelmini, Phase change materials and their application to nonvolatile memories, Chem. Rev. 110 (1) (2010) 240–267.
4. M. Wuttig, N. Yamada, Phase-change materials for rewritable data storage, Nat. Mater. 6 (11) (2007) 824–832.
5. Pumlianmunga, K. Ramesh, SET and RESET states of As2Se3 doped GeTe4 bulk glasses probed by Raman spectroscopy, J. Appl. Phys. 120 (21) (2016).
6. R. Huang, et al., Phase-change memory properties of electrodeposited Ge-Sb-Te thin film, Nanoscale Res. Lett. 10 (1) (2015) 4–10.
7. R. Todorov, J. Tasseva, T. Babeva, Thin chalcogenide films for photonic applications, in: Photonic Cryst. - Innov. Syst. Lasers Waveguides, Intech, Croat, 2012, p. 143.
8. N. Mateleshko, V. Mitsa, S. Sikora, Optical properties of SnO2-As2Se3-ZnS(Mn, Cu)-Al structure with intermediate chalcogenide-glass layer, Ukrainian J. Phys. Opt. 4 (3) (2003) 135–138.
9. E. Nicoletti, et al., As2S3 photonic crystals for spontaneous emission control of PbSe\CdSe core-shell quantum dots, in: In *2009 9th IEEE Conference on Nanotechnology*, IEEE-NANO), 2009, pp. 717–718.
10. B. Suthar, A. Bhargava, Chalcogenide photonic crystal filters for optical communication, AIP Conf. Proc. 1393 (2011) 273–275.
11. H. Saghaei, A. Zahedi, R. Karimzadeh, F. Parandin, Superlattices and Microstructures Line defects on As2Se3-Chalcogenide photonic crystals for the design of all-optical power splitters and digital logic gates, Superlattice Microstruct. 110 (2017) 133–138.
12. D.V. Martyshkin, V.V. Fedorov, J.T. Goldstein, S.B. Mirov, Mid-IR lasing of Cr: ZnSe/As2S3:As2Se3 composite materials, Solid State Lasers XX: Technol. Devices 7912 (2011) 79121l.
13. W. Fischer, "A second note on the term 'chalcogen, J. Chem. Educ. 78 (10) (2001) 1333.
14. T. Kohoutek, et al., Surface morphology of spin-coated As-S-Se chalcogenide thin films, J. Non-Cryst. Solids 353 (13–15) (2007) 1437–1440. SPEC. ISS.
15. I. Chung, M.G. Kanatzidis, Metal chalcogenides: a rich source of nonlinear optical materials, Chem. Mater. 26 (1) (2014) 849–869.
16. V. Pandey, S.K. Tripathi, A. Kumar, A study of optical parameters of amorphous Se70Te30-XAgX thin films before and after heat treatment, J. Optoelectron. Adv. Mater. 10 (2007).
17. J. Fick, E.J. Knystautas, A. Villeneuve, F. Schiettekatte, S. Roorda, K.A. Richardson, High photoluminescence in erbium-doped chalcogenide thin films, J. Non-Cryst. Solids 272 (2–3) (2000) 200–208.
18. S. Song, et al., Phase-change properties of GeSbTe thin films deposited by plasma-enhanced atomic layer deposition, Nanoscale Res. Lett. 10 (1) (2015) 3–7.
19. N. Carlie, et al., Measurement of the refractive index dispersion of As2Se3 bulk glass and thin films prior to and after laser irradiation and annealing using prism coupling in the near- and mid-infrared spectral range, Rev. Sci. Instrum. 82 (5) (2011).
20. A. Zakery, Pulsed laser deposition of chalcogenide films for nonlinear photonic applications, J. Optoelectron. Adv. Mater. 7 (3) (2005) 1143–1155.
21. Y. Zou, et al., Effect of annealing conditions on the physio-chemical properties of spin-coated As_2Se_3 chalcogenide glass films, Opt. Mater. Express 2 (12) (2012)
22. R.A. Castro, V.A. Bordovsky, G.I. Grabko, in: Investigation of the Processes of Charge Transfer and Charge Accumulation in as 2 Se 3 Amorphous Layers Prepared by Different Methods, vol. 35, 2009, pp. 43–44, 1.
23. Y. Lai, F. Liu, J. Li, Z. Zhang, Y. Liu, Nucleation and growth of selenium electrodeposition onto tin oxide electrode, J. Electroanal. Chem. 639 (1–2) (2010) 187–192.
24. J. Orava, T. Kohoutek, T. Wagner, Deposition techniques for chalcogenide thin films, in: In *Chalcogenide Glasses*, Elsevier, 2014, pp. 265–309.
25. V.S. Shiryaev, M.F. Churbanov, Preparation of High-Purity Chalcogenide Glasses, *Chalcogenide Glas*, 2013, pp. 3–35.
26. W.A. King, A.G. Clare, W.C. LaCourse, Laboratory preparation of highly pure As2Se3glass, J. Non-Cryst. Solids 181 (3) (1995) 231–237.
27. Y. Azhniuk, et al., In-doped As2Se3 thin films studied by Raman and X-ray photoelectron spectroscopies, Appl. Surf. Sci. 471 (2018) 943–949.
28. T. Hristova-Vasileva, I. Bineva, A. Dinescu, M. Danila, D. Arsova, "As2Se3 thin films deposited by frequency assisted thermal evaporation – morphology and structure, J. Phys. Conf. Ser. (2017) 3–9.
29. W.N. Haynes, R.L. David, J.B. Thomas, CRC Handbook of Chemistry and Physics, 97th Editi, vol. 91, 2017.
30. A. Bowen, J. Li, J. Lewis, K. Sivaramakrishnan, T.L. Alford, S. Iyer, The properties of radio frequency sputtered transparent and conducting ZnO:F films on polyethylene naphthalate substrate, Thin Solid Films 519 (6) (2011) 1809–1816.

31. O.A. El-gammal, A.F. Al-hossainy, S.A. El-brashy, Spectroscopic, DFT, optical band gap, powder X-ray diffraction and Bleomycindependant DNA studies of Co(II), Ni (II) and Cu(II) complexes derived from macrocyclic Schiff base, J. Mol. Struct. 1165 (Ii) (2018) 177–195.
32. S. Speakman, Estimating crystallite size using XRD, MIT Cent. Mater. Sci. Eng. (2015) 1–66.
33. V. Kovanda, M. Vl, "Structure of as – Se and as – P – Se glasses studied by Raman spectroscopy, J. Non-Cryst. Solids 326 (327) (2003) 88–92.
34. V.I. Mikla, "Distinct topological regimes in binary AsxSe1- x glasses, J. Phys. Condens. Matter 9 (43) (1997) 9209–9217.
35. E.I. Kamitsos, M.S. Iovu, C. Varsamis, P. Boolchand, M. Popescu, Raman spectra of AsxSe100-x and As40Se60 glasses doped with metals, Chalcogenide Lett. 2 (3) (2005) 21–25.
36. E.I. Kamistos, et al., Structure of arsenic selenide glasses by Raman and 77 Se NMR with a multivariate curve resolution approach, J. Non-Cryst. Solids 447 (2016) 322–328.
37. M. Behera, S. Behera, R. Naik, Optical band gap tuning by laser induced Bi di ff usion into as 2 Se 3 fi lm probed by spectroscopic, RSC Adv. 7 (2017) 18428–18437.
38. M.S. Dresselhaus, Solid State Physics Part II, 2001.
39. G. Yang, et al., "Correlation between structure and physical properties of chalcogenide glasses in the as x Se 1 □ x system, Phys. Rev. B 82 (19) (2010) 1–8.
40. P.O. Offor, et al., The Characteristics and Wettability Response of Spray- Synthesized ZnS Films Complexed with glycine, " *Surfaces and Interfaces*, 2019.
41. N. Khemiri, M. Kanzari, Determination and analysis of optical constants and dispersion energy parameters of Zn(S,O) thin films, Mater. Chem. Phys. 214 (2018) 185–191.
42. N.M. Saeed, Structural and Optical Properties of ZnS Thin Films Prepared by Spray Pyrolysis Technique, vol. 14, J. Al-Nahrain Univ., 2011, pp. 86–92, 2.
43. R. Chauhan, A.K. Srivastava, A. Tripathi, K.K. Srivastava, Linear and nonlinear optical changes in amorphous As2Se3thin film upon UV exposure, Prog. Nat. Sci. Mater. Int. 21 (3) (2011) 205–210.
44. J. Kennedy, P.P. Murmu, J. Leveneur, A. Markwitz, J. Futter, Controlling preferred orientation and electrical conductivity of zinc oxide thin films by post growth annealing treatment, Appl. Surf. Sci. 367 (2016) 52–58.
45. V. Prince, R. Singh, M. Zulfequar, A. Kumar, P.K. Dwivedi, Electrical and optical properties of solution phase deposited As2S3 and As2Se3 chalcogenide thin films: a comparative study with thermally deposited films, J. Non-Cryst. Solids 476 (2017) 46–51. September.
46. P.O. Offor, et al., Structural, morphological and optical properties of spray-formed silver-doped zinc sulphide thin films, Optik Int. J. Light Electron Opt. 185 (2019) 519–528.
47. A.S. Rajashekharaiah, et al., NUV light-induced visible green emissions of Erbium-doped hierarchical Bi 2 Zr 2 O 7 structures, Opt. Mater. 95 (2019) 109237.
48. D.R. Patwari, B. Eraiah, Luminescence properties of erbium doped sodium barium borate glass with silver nanoparticles Luminescence properties of erbium doped sodium barium borate glass with silver nanoparticles, IOP Conf. Ser. Mater. Sci. Eng. 310 (2018).
49. N. Singh, K. Jun, B.K. Das, Synthesis and optical properties of CdS/PVA nanocomposites, Mater. Chem. Phys. 94 (2005) 454–459.
50. D.C. Onwudiwe, A.D. Mohammed, C.A. Strydom, D.A. Young, A. Jordaan, Superlattices and Microstructures Colloidal synthesis of monodispersed ZnS and CdS nanocrystals from novel zinc and cadmium complexes, Superlattice Microstruct. 70 (2014) 98–108.